Independence and interdependencies among global ocean color properties: Reassessing the bio-optical assumption

David A. Siegel, Stéphane Maritorena, and Norman B. Nelson
Institute for Computational Earth System Science, University of California, Santa Barbara, California, USA

Michael J. Behrenfeld[1]
Goddard Space Flight Center, Greenbelt, Maryland, USA

Received 11 June 2004; revised 25 November 2004; accepted 23 March 2005; published 20 July 2005.

[1] The bio-optical assumption states that ocean optical properties should covary with the chlorophyll concentration. However, chlorophyll is not the only constituent capable of absorbing and scattering light as phytoplankton, detrital particles, colored dissolved organic material (CDOM), and suspended solids all contribute independently to ocean color. Here we employ a semi-analytical ocean color algorithm, the Garver-Siegel-Maritorena model (GSM01), to decompose ocean color imagery from the Sea-viewing Wide Field of view Sensor (SeaWiFS) into optically relevant components for phytoplankton absorption (related to the chlorophyll concentration, Chl), colored non-algal absorption and particulate backscatter. Semi-analytical Chl retrievals are consistent with available open ocean observations but show important differences compared with the standard SeaWiFS algorithm (OC4v4). These differences may be accounted for by the absorption due to colored detrital materials (CDM; the sum of colored dissolved organic material and detrital particulates). Values of CDM are a large and variable fraction of the total non-water absorption at 440 nm varying from 30 to 40% in the subtropical gyres to more than 60% at high latitudes. Retrievals of particulate backscatter (BBP) vary comparatively little. In the tropical and subtropical oceans, changes in BBP are largely unrelated to Chl, while at higher latitudes, BBP increases mirror changes in Chl. For much of the ocean, alterations in the relationship between BBP and Chl are consistent with a physiological response by phytoplankton to changes in mixed layer light, nutrients, and temperature. Regional scale correspondences among the three ocean color properties illustrate both independent and interdependent variations which can be explained by assessing the regional scale forcing mechanisms driving changes in ocean color properties.

Citation: Siegel, D. A., S. Maritorena, N. B. Nelson, and M. J. Behrenfeld (2005), Independence and interdependencies among global ocean color properties: Reassessing the bio-optical assumption, *J. Geophys. Res.*, *110*, C07011, doi:10.1029/2004JC002527.

1. Introduction

[2] Satellite ocean color sensors, such as the Sea-viewing Wide Field of view Sensor (SeaWiFS), provide, for the first time, high-quality observations of the biological and biogeochemical properties of the ocean on local to global space and timescales [e.g., *McClain et al.*, 2004]. Central to the application and interpretation of ocean color imagery is the so-called "bio-optical assumption" [e.g., *Smith and Baker*, 1978a, 1978b], which states that the optical properties of a water mass covary to first order with phytoplankton pigment (chlorophyll) biomass [e.g., *Gordon and Morel*, 1983; *Morel and Maritorena*, 2001]. The present generation of bio-optical algorithms, which relate the ocean color spectrum to in-water properties, depends on the validity of this assumption [e.g., *O'Reilly et al.*, 1998].

[3] Simply, there are more optically relevant materials in a sample of seawater than just phytoplankton chlorophyll. Recent work suggests that colored dissolved and detrital particulate material absorption (CDM) and particulate backscattering (BBP) contribute significantly to ocean optical signals [e.g., *Roesler and Perry*, 1995; *Garver and Siegel*, 1997; *Stramski et al.*, 1999; *Carder et al.*, 1999; *Maritorena et al.*, 2002; *Siegel et al.*, 2002b; *Loisel et al.*, 2002; *Maritorena and Siegel*, 2005]. The present generation of remote sensing algorithms can separate the magnitude of the inherent optical properties (IOPs) of the upper ocean from spectral observations of ocean color. Typically, these IOPs are: phytoplankton absorption (APH; a known function of the chlorophyll concentration, Chl), colored dissolved and detrital material absorption (CDM), and particulate backscattering coefficients (BBP). With these three ocean color products, an opportunity now exists to evaluate the validity

[1]Now at Department of Botany and Plant Pathology, Oregon State University, Corvallis, Oregon, USA.

0148-0227/05/2004JC002527

Table 1. Processes and Environmental Forcings Regulating Global Ocean Color Properties

Property	What Is Sensed	Regulating Process	Forcing Mechanism
BBP particulate backscatter	particle biomass; suspended sediments	primary production; terrestrial inputs	nutrient input/upwelling; land-ocean interactions; dust deposition?
Chl chlorophyll concentration	chlorophyll biomass	primary production; physiological changes of phytoplankton C:Chl	nutrient input/upwelling; growth irradiance and nutrient stress
CDM colored detrital materials	CDOM detrital particulates	heterotrophic production; photobleaching; terrestrial inputs	upwelling/entrainment; UV light dosage; land/ocean interactions

of the ''bio-optical assumption'' at global spatial and climatological timescales.

[4] If the bio-optical assumption holds, the above three ocean color properties should all covary. This assumption will break down if one of the IOPs varies independently such as would occur if the IOPs respond differentially to a given environmental perturbation. For example, recent observations of open ocean CDM variations indicate that photobleaching is the dominant degradative process, while heterotrophic microbial activity appears to be the production pathway [e.g., *Nelson et al.*, 1998; *Siegel et al.*, 2002b; *Nelson and Siegel*, 2002; *Nelson et al.*, 2004a]. Accordingly, satellite CDM values should reflect the combined processes of photobleaching (i.e., low CDM in high light, shallow mixing regions) and microbial secondary production which is tied through the microbial loop to overall rates of primary production (see Table 1). While the latter of these processes may link changes in CDM to variations in Chl, the former at times may not. The discharge of CDM-rich freshwater plumes may also have important regional effects on CDM with little correspondence in Chl [*Siegel et al.*, 2002b]. On the other hand, if detrital particulate absorption were to dominate CDM variability, a high degree of correspondence with Chl would be expected. Hence differences in the regulating processes can create divergent patterns in CDM and Chl which violate the bio-optical assumption.

[5] Particulate backscattering (BBP) is a measure of light scattering by particles and a proxy for suspended particle abundance [e.g., *Gordon and Morel*, 1983; *Stramski and Kiefer*, 1991; *Morel and Ahn*, 1991; *Loisel and Morel*, 1998; *Behrenfeld and Boss*, 2003; *Stramski et al.*, 2004]. The slope of the particle size spectrum changes little in the open ocean [e.g., *Bader*, 1970; *Stramski and Kiefer*, 1991; *Stramski et al.*, 2004]. Hence changes in BBP should be, to first order, related to changes in phytoplankton particulate biomass [e.g., *Behrenfeld and Boss*, 2003; *Behrenfeld et al.*, 2005]. Extreme changes in the planktonic size and community distributions as well as contributions from suspended mineral particles can complicate this situation which will occur in near-coastal environments [e.g., *Stramski et al.*, 2004]. Elsewhere, changes in BBP and phytoplankton particulate biomass should be well related.

[6] This suggests that changes in the relationship between BBP and Chl should reflect changes in the phytoplankton carbon biomass to chlorophyll ratio (C:Chl). In open ocean regions, changes in C:Chl can result from two basic responses to environmental changes. The first is a ''biomass regime'' where increases in Chl, such as will occur in a phytoplankton bloom, mirror proportional changes in phytoplankton carbon biomass as estimated by BBP. The second occurs when phytoplankton adjust their intracellular pigment content in response to ambient light, nutrient, and temperature stresses [e.g., *Falkowski*, 1984; *Geider et al.*, 1998; *Behrenfeld et al.*, 2002]. This ''photoacclimation regime'' will create a decoupling in the Chl and BBP response as high light and high nutrient stresses correspond to high phytoplankton carbon to chlorophyll (C:Chl) ratios [*Behrenfeld et al.*, 2005]. These differences have long been apparent in vertical profiles of chlorophyll and optical proxies of particulate carbon [e.g., *Kitchen and Zaneveld*, 1990; *Loisel and Morel*, 1998; *Fennel and Boss*, 2003]. Recently, these same physiological changes have been diagnosed across regions and seasons using the same ocean color data presented here [*Behrenfeld et al.*, 2005]. As an example, monthly averages of BBP and Chl along a meridional transect across the North Atlantic Ocean (along 30°W) clearly demonstrate two basic regimes in the BBP-Chl relationship (Figure 1a). For Chl levels greater than $\sim$0.15 mg m^{-3}, changes in Chl and BBP occur in rough concert illustrating dominance by a ''biomass regime'' for the two subarctic locations (50°N and 40°N along 30°W). However, changes in BBP are not obviously related to Chl for the two subtropical locations (Figure 1a). Evidence for this ''photoacclimation'' mode can be seen by plotting the BBP to Chl ratio versus the mean irradiance for the mixed layer, I_g, for each month (Figure 1b). Values of BBP/Chl at 30°N and 40°N are a strong function of growth irradiance indicating the photoacclimation of cellular chlorophyll concentrations to ambient light levels [*Behrenfeld et al.*, 2005]. The two northern locations (50°N and 60°N) do not show this same dependence on light. The stronger response of the BBP/Chl ratio to light at 30°N compared with 40°N suggests that the C:Chl ratio is responding to differences in the ambient nutrient concentrations between the two sites [*Nelson et al.*, 2004b]. A global analysis of the relationship between BBP and Chl and its importance for the modeling primary production is given by *Behrenfeld et al.* [2005].

[7] The driving relationships described above suggest that both dependent and independent behaviors of the three ocean color properties are expected. An encapsulation of the mechanisms driving these changes and relevant environmental forcings is provided in Table 1. Although this provides an incomplete listing of all the processes, it presents some simple hypotheses for the regulation of global ocean color properties. To test these hypotheses, we apply a semi-analytical ocean color algorithm to global observations from the SeaWiFS ocean color satellite mission [*McClain et al.*, 2004]. In the following sections, we introduce and validate methods for assessing global ocean color properties and present observations from the first 5 years of the SeaWiFS mission. These analyses are used to test hypotheses of the driving mechanisms regulating

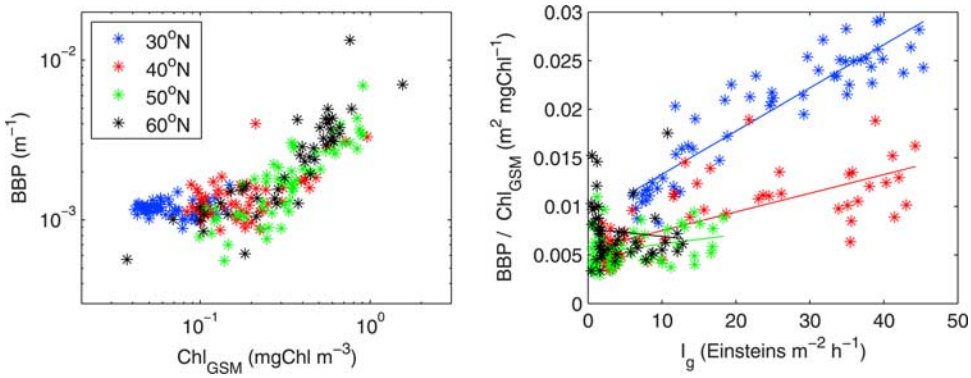

Figure 1. Example of the relationships between Chl_{GSM} and BBP across the North Atlantic Ocean. (a) Monthly averages of Chl_{GSM} and BBP taken at 30°N (blue), 40°N (red), 50°N (green), and 60°N (black) on a transect centered at 30°W across the North Atlantic Ocean. (b) The ratio of Chl_{GSM} to BBP taken at 30°N (blue), 40°N (red), 50°N (green), and 60°N (black) on a transect centered at 30°W plotted as a function of the mean mixed layer growth irradiance, I_g [following *Behrenfeld et al.*, 2005]. Regression slopes for all four latitude locations are shown where regression coefficients (r values) decrease from 30°N to 60°N along 30°W (r^2 = 0.84, 0.51, 0.08, and 0.01). Data methods for determination of Chl_{GSM} and BBP are given in section 2. Mean mixed layer growth irradiance, I_g, is calculated knowing from determinations of incident PAR flux, mixed layer depth (FNMOC product; https://www.fnmoc.navy.mil) and attenuation coefficients for PAR (see *Behrenfeld et al.* [2005] or *Siegel et al.* [2002a] for details).

ocean color property variations and to evaluate the validity of the bio-optical assumption for the global ocean.

2. Data and Methods

[8] Global imagery from the Sea-viewing Wide Field of View Sensor (SeaWiFS) are analyzed using the Garver-Siegel-Maritorena (GSM01) semi-analytical ocean color algorithm [*Garver and Siegel*, 1997; *Maritorena et al.*, 2002]. The GSM01 algorithm decomposes observations of water-leaving radiance into a set of ocean color properties which describe the optical state of the upper ocean; the chlorophyll concentration, Chl, the colored dissolved organic and detrital material absorption coefficient at 440 nm, CDM, and the particulate backscatter coefficient at 440 nm, BBP. Briefly, the GSM01 algorithm inverts observations of the normalized water leaving radiance spectrum, $L_{wN}(\lambda)$, to estimate Chl, CDM, and BBP following

$$\hat{L}_{wN}(\lambda) = \frac{t\,F_o(\lambda)}{n_{sw}^2} \sum_{m=1}^{2} g_m \cdot \left(\frac{b_{bw}(\lambda) + \underline{BBP}\,(\lambda_o/\lambda)^{\eta}}{b_{bw}(\lambda) + \underline{BBP}\,(\lambda_o/\lambda)^{\eta} + a_w(\lambda) + \underline{Chl}\,a_{ph}^{*}(\lambda) + \underline{CDM}\exp(-S(\lambda-\lambda_o))} \right)^{m}, \quad (1)$$

where the reference wavelength, λ_o, is 440 nm and the parameters to be retrieved (Chl, CDM, BBP) are underlined. In application of equation (1), values of backscattering and absorption coefficients for pure water ($b_{bw}(\lambda)$ and $a_w(\lambda)$), optical closure constants (g_m), downwelling irradiance at the top-of-the-atmosphere ($F_o(\lambda)$), the air-sea transmission factor (t), and the real part of the seawater index of refraction (n_{sw}) are all known. Terms for the chlorophyll specific phytoplankton absorption spectrum, $a_{ph}^{*}(\lambda)$, and spectral slopes for the particulate backscattering coefficient (η) and colored detrital materials (S) were specified through an optimal tuning against a global data set [*Maritorena et al.*, 2002]. Comparison of GSM01 Chl retrievals against the global in situ data set are excellent (r^2 = 0.910 slope = 0.97, N = 1075) and at least as good as the operational SeaWiFS algorithm (OC4v4; r^2 = 0.919; slope = 1.04; N = 1075). Likewise, comparison of the GSM01 and in situ CDM data set indicates excellent agreement (r^2 = 0.870, slope = 1.01; N = 1075). Hindcasts between the GSM01 BBP results and the BBP proxy used in developing the GSM01 algorithm are only fair (r^2 = 0.426, slope = 0.85; N = 1071).

[9] The GSM01 model was applied to global SeaWiFS imagery of normalized water-leaving radiance ($L_{wN}(\lambda)$; 8-day composite fields sampled at 9 km for wave bands centered on 412, 443, 490, 510, 555 and 670 nm). Observations from the first 5 years of the SeaWiFS satellite mission ("reprocessing 4") are used (http://seawifs.gsfc.nasa.gov/SEAWIFS/RECAL/Repro4/) and monthly averages are constructed on a 1/3° spatial grid. In an earlier study, *Siegel et al.* [2002b] used SeaWiFS data from "reprocessing 3." "Reprocessing 4" updated several radiometric calibration coefficients which increased retrievals of $L_{wN}(412)$ and reduced CDM values. Fortunately, the basic CDM patterns and interpretations presented by *Siegel et al.* [2002b] are unaffected by this difference in satellite radiometric calibration.

[10] The availability of field data coincident with the SeaWiFS mission provides the opportunity for an end-to-end validation of the GSM01 retrievals. These matchup data are available for chlorophyll *a* concentration, to a lesser extent for water-leaving radiance and CDM, and very infrequently for BBP. Detailed matchup comparisons of satellite retrievals and field determinations of chlorophyll *a* concentration are presented here. Field-satellite data matchups were constructed using a nine-pixel median value from local area coverage (LAC) SeaWiFS imagery with a

Table 2. Validation Statistics for Chlorophyll *a* Concentration Retrievals

	OC4v4 Versus In Situ	GSM01 Versus In Situ	OC4v4 Versus In Situ, Z > 1000 m	GSM01 Versus In Situ, Z > 1000 m
N	358	316	59	59
r^2	0.760	0.657	0.747	0.785
Slope	0.919	0.767	0.935	0.927
Intercept	−0.007	−0.234	−0.070	−0.104
RMS	0.258	0.334	0.204	0.186
BIAS	0.026	−0.132	−0.011	−0.038

time of difference of 3 hours or less (see http://seabass.gsfc.nasa.gov/matchup_results.html). A total number of 358 matchups are available for validating the OC4v4 and GSM01 model results (Table 2). Simple regression statistics for the in situ versus satellite retrieved chlorophyll determinations show that the SeaWiFS standard OC4v4 algorithm is more accurate than the GSM01 when applied over a wide range of ocean conditions (Table 2). However, of the 358 total matchups, only 59 of them are available in deep waters (>1000 m) far from continental margins. These open ocean data are most relevant to the large-scale processes which are the focus of this paper. When matchups are compared only for these deep water sites, statistical validation metrics for the two algorithms are nearly identical (Table 2). On the basis of available matchup data, GSM01 and OC4v4 have equivalent performance characteristics for assessing Chl in the open ocean (Table 2).

[11] Semi-analytical ocean color algorithms, such as GSM01, are more sensitive to errors in the $L_{wN}(\lambda)$ retrievals than are ratio algorithms (compare OC4v4 [*O'Reilly et al.*, 1998]). Hence the degraded performance of the GSM01 algorithm in coastal environments is not unexpected as its performance is dependent on the quality of the $L_{wN}(\lambda)$ retrievals for all six SeaWiFS wave bands. If the input $L_{wN}(\lambda)$ spectrum is in serious error, the GSM01 algorithm may not converge (which is why there are fewer matchup data points available for GSM01 retrievals compared with OC4v4 in Table 2). Poor performance of the SeaWiFS atmospheric correction algorithm in coastal zones is a well known problem [e.g., *Kahru and Mitchell*, 1999; *Otero and Siegel*, 2004] and likely caused by the complex nature of atmospheric absorbing and scattering aerosols from mixtures of continental, urban, and marine air masses and the relatively simple methods of atmospheric correction used on an operational basis [e.g., *Chomko et al.*, 2003].

[12] A preliminary matchup between all available field and satellite CDM observations showed good correspondence (r^2 = 0.610; power law slope = 1.146; N = 112 following *Siegel et al.* [2002b]). The time control (8 day) for these comparisons is not as strict as the above SeaWiFS Chl analysis reflecting the scarcity of CDM observations, particularly for the open ocean. Recently, one of us (N. B. N.) sampled CDOM profiles from three meridional transects across the North Atlantic Ocean. These observations covered a longitude range from 20°W to 70°W and a latitude range from 7°N to 62°N (Repeat Hydrography Cruises A16N, A20 and A22). A total of 111 profiles had corresponding valid SeaWiFS observations. To account for subsurface CDOM that could be "seen" by ocean color sensors in clear water, the in situ profiles were averaged over the top 50 m (roughly the $1/\underline{K_d}(412)$ depth). The absorption coefficients found by both methods ranged from near zero to over 0.05 m^{-1}. Overall, there was good correspondence between the GSM01 estimated CDM and the in situ CDOM absorption coefficient at 443 nm (r^2 = 0.65; N = 111). The linear regression slope was 1.16, with an intercept of 0.003 m^{-1}, indicating approximately a 15% overestimation of CDOM absorption by the GSM algorithm. The overestimation may be simply due to the fact that detrital absorption is not accounted for in this comparison.

[13] The situation for in situ validation is far worse for BBP as very few in situ observations are available. An inspection of the SeaBASS data archive found that nearly all of the available BBP data were from turbid, coastal areas. Hence we cannot perform a detailed system validation of the BBP retrieval and need to rely on a model-to-model validation of the product. The GSM01 algorithm BBP retrievals compare only fair with the "quasi-real" estimates of BBP used to tune the GSM01 model (r^2 = 0.426; N = 1071 [*Maritorena et al.*, 2002]. However, the BBP "observations" used by *Maritorena et al.* [2002] were generated with the *Morel and Maritorena* [2001] chlorophyll-based algorithm. A similar comparison using the *Carder et al.* [1999] reflectance-based BBP model are much more encouraging (r^2 = 0.624; N = 1072). Applying the *Carder et al.* [1999] BBP algorithm to SeaWiFS imagery produces similar spatial/temporal patterns as are found with GSM01 (data not shown). Statistical comparisons are excellent (r^2 values are greater than 0.83 between given monthly mean, global BBP fields). The correspondence between the *Carder et al.* [1999] BBP estimate and the present one is encouraging and suggests that chlorophyll-based models for BBP may not be valid. Again, this will require coincident field observations.

3. Time-Space Variability of Global Ocean Color Properties

3.1. Five-Year Global Climatological Ocean Color Property Distributions

[14] The SeaWiFS operational algorithm (Chl_{WiFS}) and the GSM01 model (Chl_{GSM}) both yield surface chlorophyll fields exhibiting high values at high latitudes, lower values in the tropics, and the lowest values in subtropical gyres (Figures 2a and 2b). These well-established patterns illustrate the role of gyre-scale nutrient upwelling and downwelling on global productivity [e.g., *Sverdrup*, 1955; *Yoder et al.*, 1993]. Both models also give high chlorophyll estimates in marginal seas and for coastal regions, although Chl_{WiFS} values are noticeably higher than Chl_{GSM} (Figures 2a and 2b). Overall, correspondence between the two algorithms is fair (r = 0.833), but Chl_{WiFS} gives considerably higher retrievals for the northern latitude and coastal oceans. It is unclear which of these patterns is correct as the data available to validate this are lacking [e.g., *Claustre and Maritorena*, 2003]. It is possible that these differences are created through limitations in the data sets used to develop satellite algorithms (see below).

[15] The mission mean CDM field (Figure 2c) shows the result of the light-driven cycling of CDOM, where satellite-sensed CDM values are lower in the tropics and higher toward the poles [*Siegel et al.*, 2002b; *Nelson and*

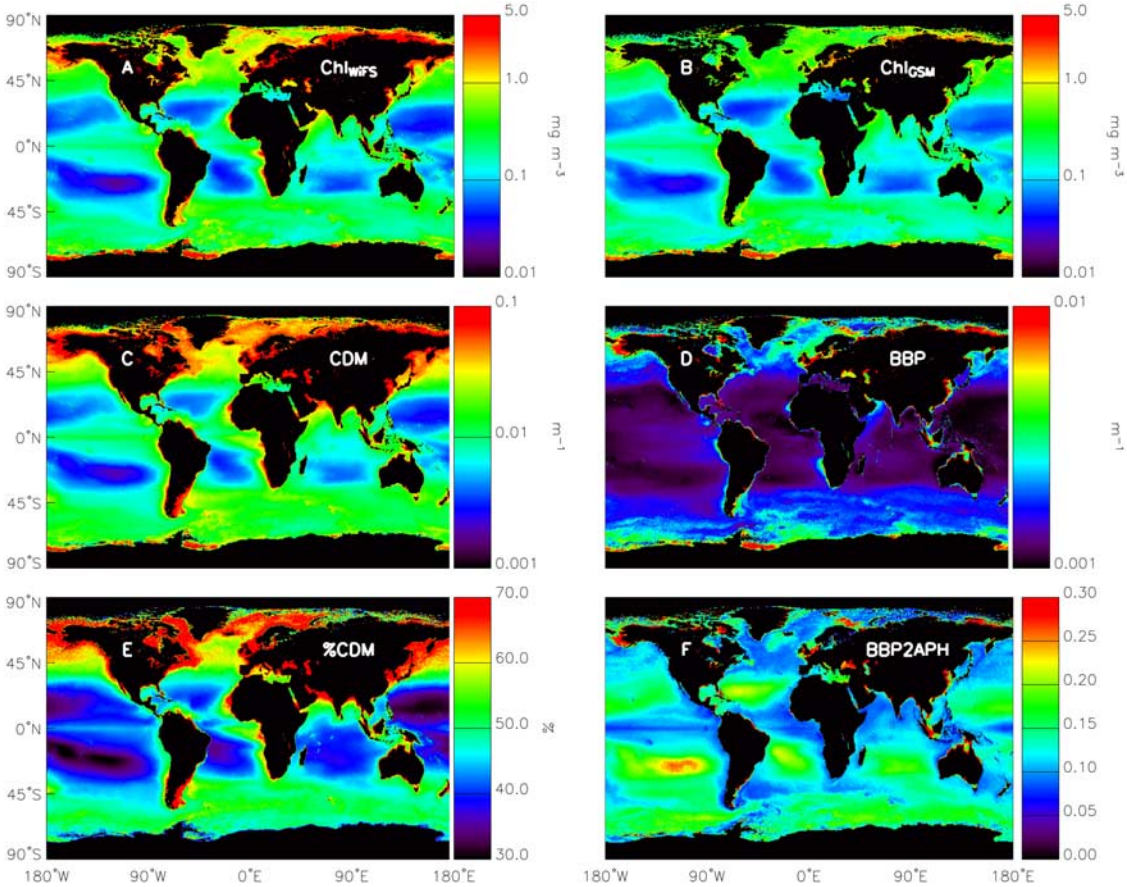

Figure 2. Five-year mean fields of (a) chlorophyll concentration from the operational SeaWiFS algorithm (OC4v4) (Chl_{WiFS}), (b) chlorophyll concentration from GSM01 (Chl_{GSM}), (c) colored dissolved and detrital particulate material absorption at 440 nm (CDM), (d) particulate backscattering coefficient at 440 nm (BBP), (e) the percent non-water absorption at 440 nm driven by CDM (%CDM; equation (2)) and (f) a comparison of the retrieved backscatter to particulate absorption at 440 nm (BBP2APH; equation (3)). SeaWiFS level 3 images of water-leaving radiance spectra are used to develop these 5-year climatologies of ocean color properties.

Siegel, 2002]. On a regional scale, regions with shallow mixed layers and downwelling Ekman pumping (compare subtropical gyres) have lower CDM values than regions with seasonally deep mixed layer depths and upwelling Ekman fluxes (compare subarctic gyres). This suggests that photolysis driven by the mixed layer averaged light-dose of ultraviolet radiation is an important process regulating the global CDM distribution as viewed from space. Further, values of CDM clearly demarcate regions where consistent large-scale upwelling and downwelling motions are observed. High CDM retrievals are found in regions of equatorial upwelling and the subarctic gyres while low values are found throughout the subtropics. This suggests that the vertical advection and mixing of subsurface CDOM concentrations to the mixed layer modifies the meridional pattern of CDM bleaching and has an important role in setting the global patterns [e.g., *Siegel et al.*, 2002b].

[16] The processes producing CDM at depth are fundamentally different than those driving changes in chlorophyll pigment concentrations [*Siegel and Michaels*, 1996; *Nelson et al.*, 1998, 2004a; *Nelson and Siegel*, 2002; *Siegel et al.*, 2002b]. However, their surface manifestations are both modulated by large-scale vertical advection resulting in roughly similar global patterns. There are also important differences between the Chl and CDM distributions. For example, large interhemispherical differences are found for CDM, with much higher CDM retrievals at high latitudes of the Northern Hemisphere ocean than at high latitudes in the Southern Hemisphere. Differences between Chl_{WiFS} and Chl_{GSM} in the northern high latitude oceans are in a sense "compensated" for by CDM values in the GSM01 model. That is, the operational algorithm (Chl_{WiFS}) may be mistakenly assessing chlorophyll concentrations due to the presence of CDM [e.g., *Carder et al.*, 1991; *Siegel and Michaels*, 1996], potentially biasing SeaWiFS chlorophyll retrievals high. Conversely for extremely low Chl regions, values of Chl_{GSM} are generally larger than Chl_{WiFS}. The resolution of these differences is not possible at this time as very few radiometric observations are available from either high latitude or very blue regions of the oceans [e.g., *Claustre and Maritorena*, 2003], and it remains that the observed differences may simply be due to limitations in the "global" data set used to develop ocean color algorithms.

[17] Unlike the Chl or CDM distributions, the BBP distribution has little obvious hemispherical difference (Figure 2d). Further, the magnitude of global scale BBP variations are small (factor of ~3) compared with Chl_{GSM} (Figure 2b; factor of roughly 20) and CDM (Figure 2c; factor of 10 or so). With the exception of coastal regions, BBP values are low (0.001 to 0.0015 m^{-1}) throughout the tropical and subtropical oceans. Higher BBP values (BBP $\geq$ 0.003 m^{-1}) are found in regions with enhanced chlorophyll biomass and poleward of ~40° latitude (Figure 2d). Extreme BBP values (>0.006 m^{-1}) are restricted to coastal areas and marginal seas, such as the Bering, Ross, Black, and North seas. In these regions, optical properties are likely controlled by abiotic components (sediments, detritus, etc.) and reflect the importance of land-ocean interactions. Blooms of particular phytoplankton taxa, such as coccolithophores, may also significantly influence BBP in these regions [e.g., *Brown and Yoder*, 1994].

3.2. Relative Contributions of Ocean Color Properties

[18] To assess the relative importance of CDM and BBP to the ocean color properties of the upper ocean, simple ratio functions are constructed. For example, the contribution of CDM to the total non-water absorption coefficient at 440 nm can be measured using

$$\%\mathrm{CDM} = \frac{100\,\mathrm{CDM}}{\mathrm{CDM} + \hat{a}_{ph}(440; \mathrm{Chl}_{GSM})}, \quad (2)$$

where $\hat{a}_{ph}(440;Chl_{GSM}) = 0.0378\ (Chl_{GSM})^{0.627}$ [*Bricaud et al.*, 1998]. The global %CDM distribution for the 5-year SeaWiFS data set is shown in Figure 2e. Climatological estimates of %CDM range from ~30 to 70% where values are smallest in the tropics and the center of the subtropical gyres while the highest %CDM retrievals are found in the high-latitude oceans (particularly in the northern latitudes). The global mean value for %CDM is 46% implying that nearly one half of the non-water absorption at 440 nm is due to CDM [*Siegel et al.*, 2002b]. The large relative contribution of CDM is somewhat surprising as 440 nm is the peak of the chlorophyll *a* absorption spectrum. For shorter wavelengths, CDM will dominate the absorption spectrum and its variability.

[19] The distribution of the climatological mean %CDM distribution shows patterns consistent with proposed mechanisms for the cycling of open ocean CDOM [*Siegel et al.*, 2002b; *Nelson and Siegel*, 2002]. Specifically, the primary source of upper layer CDM is vertical transport of subsurface CDOM and its proximate loss is due to photobleaching. Values of %CDM demarcate regions of large-scale upwelling and downwelling as relatively high determinations of %CDM are found in the subarctic gyres and for equatorial and coastal upwelling regions while low values are found throughout the subtropics. Values of %CDM also show a significant hemispherical asymmetry as noted previously (Figure 2e).

[20] The relationship between BBP and the phytoplankton absorption coefficient at 440 nm can be investigated using their ratio, or

$$\mathrm{BBP2APH} = \frac{\mathrm{BBP}}{\mathrm{APH}} = \frac{\mathrm{BBP}}{\hat{a}_{ph}(440; \mathrm{Chl}_{GSM})}, \quad (3)$$

where $\hat{a}_{ph}(440;Chl_{GSM})$ is again from *Bricaud et al.* [1998]. The BBP2APH ratio should be a good indicator for physiological changes in phytoplankton intracellular pigmentation that track changes in light, temperature, and nutrient stress [*Behrenfeld et al.*, 2005]. Simple increases in biomass that occur in concert to both Chl and BBP will result in little changes to the BBP2APH ratio. However, large changes in BBP2APH can occur owing to response to light, temperature or nutrient stress (see Figure 1). Exceptions to this should occur where particulate scattering is strongly influenced by abiotic and/or anomalous biotic factors (e.g., coastal areas, marginal seas, near river mouths, coccolithophore blooms). Aside from these spatially limited, optically complex regions, the global distribution of BBP2APH (Figure 2f) should reflect the net expression of phytoplankton C:Chl values, which increases with increasing nutrient stress, increasing light, and decreasing temperature [*Behrenfeld and Boss*, 2003; *Behrenfeld et al.*, 2005].

[21] Accordingly, high light and low nutrient conditions give rise to high BBP2APH values in the subtropical gyres, while lower mixed layer light levels and generally greater nutrient availability yields lower BBP2APH values for higher latitudes (Figure 2f). Higher BBP2APH retrievals are found in the center of the subtropical gyres and the southern ocean while lower values are found in the equatorial and subarctic oceans. This is again consistent with the control of C:Chl by the supply of new nutrients to the mixed layer (Figure 2f). In the center of subtropical gyres, new nutrient fluxes will be small owing to downwelling associated with Ekman pumping and low rates of diapycnal transport. In the southern ocean, the elevated BBP2APH estimates suggest nutrient limitation may be due to low iron concentrations. BBP2APH values are low in the North Atlantic, the monsoon regions of the Indian Ocean, and the equatorial bands of all the oceans, suggesting a role of vertical transport of nutrients in altering physiological states. Reduced values of BBP2APH are found to a lesser degree in the North Pacific Ocean (maybe due to iron supply [e.g., *Boyd*, 2002]).

[22] Deviations from this simple interpretation will occur where other processes (e.g. land-ocean interactions) influence the observed value of BBP2APH. These effects are generally restricted to coastal regions, near the mouths of large rivers and marginal seas (Bering Sea, Gulf of Carpenteria, North Sea, Yellow Sea, Mediterranean Sea, Amazon outflow region and its retroflection, etc.). This suggests a terrestrial source for these BBP signals. Patches of high BBP2APH are also found in the North Atlantic south of Iceland and Bering Sea. These values are likely due to high abundances of coccolithophores [e.g., *Brown and Yoder*, 1994]. These special cases are localized and only perturb slightly the present interpretation of physiological control on BBP2APH.

3.3. Covariation Among Ocean Color Properties

[23] Probabilities of co-occurrence provide an illustration of the degrees of independence and interdependence among the retrieved properties calculated using monthly mean values over the entire 5-year record (Figure 3). Probabilities of co-occurrence show that values of CDM generally increase with chlorophyll concentration (Figure 3a), while BBP values remain roughly independent of Chl_{GSM} and CDM, particularly when Chl is <0.15 mg m^3 and CDM is

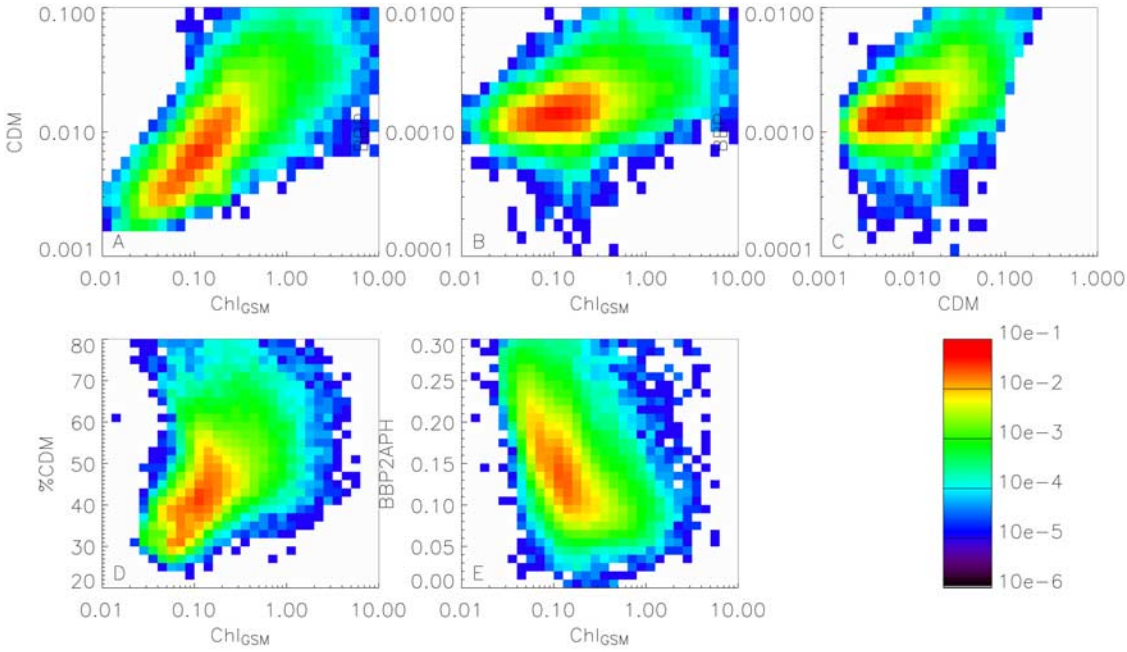

Figure 3. Two-dimensional probability density of occurrence functions for (a) Chl_{GSM} versus CDM, (b) Chl_{GSM} versus BBP, (c) CDM versus BBP, (d) Chl_{GSM} versus %CDM, and (e) Chl_{GSM} versus BBP2APH. Values are probability of occurrence scaled so that the integral over all parameter space is equal to 1. The color scale is $\log_{10}$ transformed.

<0.01 m^{-1} (Figures 3b and 3c; see also Figure 1). The linear correlation coefficient between CDM and Chl_{GSM} is significant (r = 0.75; Table 3), whereas the linear correlation between BBP and Chl_{GSM} is considerably smaller (r = 0.50; Table 3). This indicates that over wide expanses of the sea, there is fair correspondence between CDM and Chl_{GSM} whereas the BBP signal is largely independent of Chl. Specifically, the processes that alter surface expressions of CDM (photobleaching in high light conditions and upwelling of subsurface CDOM) also regulate chlorophyll pigment concentrations in a similar way but due to different processes (photoacclimation lowers cellular chlorophyll concentrations and upwelling of new nutrients raises phytoplankton pigment concentrations). The apparent decoupling between BBP and Chl is likely caused by environmental factors, such as growth irradiance and nutrient supply, regulating phytoplankton C:Chl ratios [e.g., *Behrenfeld et al.*, 2005]. Less frequently, BBP and Chl rise in concert owing to significant increases in phytoplankton biomass (Figure 3b, top right) which occurs in strongly seasonal regions.

[24] The probability distribution of co-occurrence for BBP and CDM shows relatively little correspondence between the two parameters (Figure 3c), and the correlation coefficient between them is correspondingly low (r = 0.29; Table 3) suggesting a decoupling between their regulating processes. The probabilities of co-occurrence for %CDM and BBP2APH versus Chl_{GSM} (Figures 3d and 3e) confirm many of the above patterns. In general, %CDM increases with Chl_{GSM} while BBP2APH decreases with Chl_{GSM}.

3.4. Temporal Changes in Ocean Color Properties

[25] Examples of the temporal changes in the three ocean color properties can be demonstrated in their time variation as a function of latitude along 30°W across the North Atlantic Basin (Figure 4). From 35°N to 65°N, Chl_{GSM} and CDM show significant spring increases. These variations are also clearly seen in BBP at >45°N (Figure 4). The amplitude of these seasonal cycles increases from south to north, while their phasing is latitudinally offset and suggests a northward propagation of physical forcing that is consistent with Sverdrup's critical depth hypothesis [e.g., *Sverdrup*, 1953; *Longhurst*, 1998; *Siegel et al.*, 2002a]. The spring Chl_{GSM} bloom at 60°N occurs during June–July, while the spring chlorophyll maximum at 35°N is 4 times lower with peak values during the March–April time period (Figure 4). There is an obvious northward propagation in the timing of the spring bloom from 35°N to 55°N. However, at 55°N and northward, chlorophyll blooms seem to occur simultaneously [*Siegel et al.*, 2002a]. This may be due to the coarse time resolution used and the short growing season for these high-latitude regions.

[26] All three ocean color properties, Chl_{GSM}, CDM, and BBP, show significant seasonal cycles. However, there are important differences in the magnitude and phasing of these cycles (Figure 4). For example, in the northern portion of 30°W transect, CDM often exhibits additional or time-lagged peaks compared with Chl_{GSM} or BBP. Farther to

Table 3. Correlation Coefficients (r Values) Among Global Ocean Color Properties

Value	Chl_{GSM}	CDM	BBP	%CDM	BBP2APH
Chl_{WIFS}	0.833	0.759	0.410	0.414	0.008
Chl_{GSM}		0.751	0.497	0.384	−0.131
CDM			0.290	0.716	−0.040
BBP				0.208	0.560
%CDM					−0.296

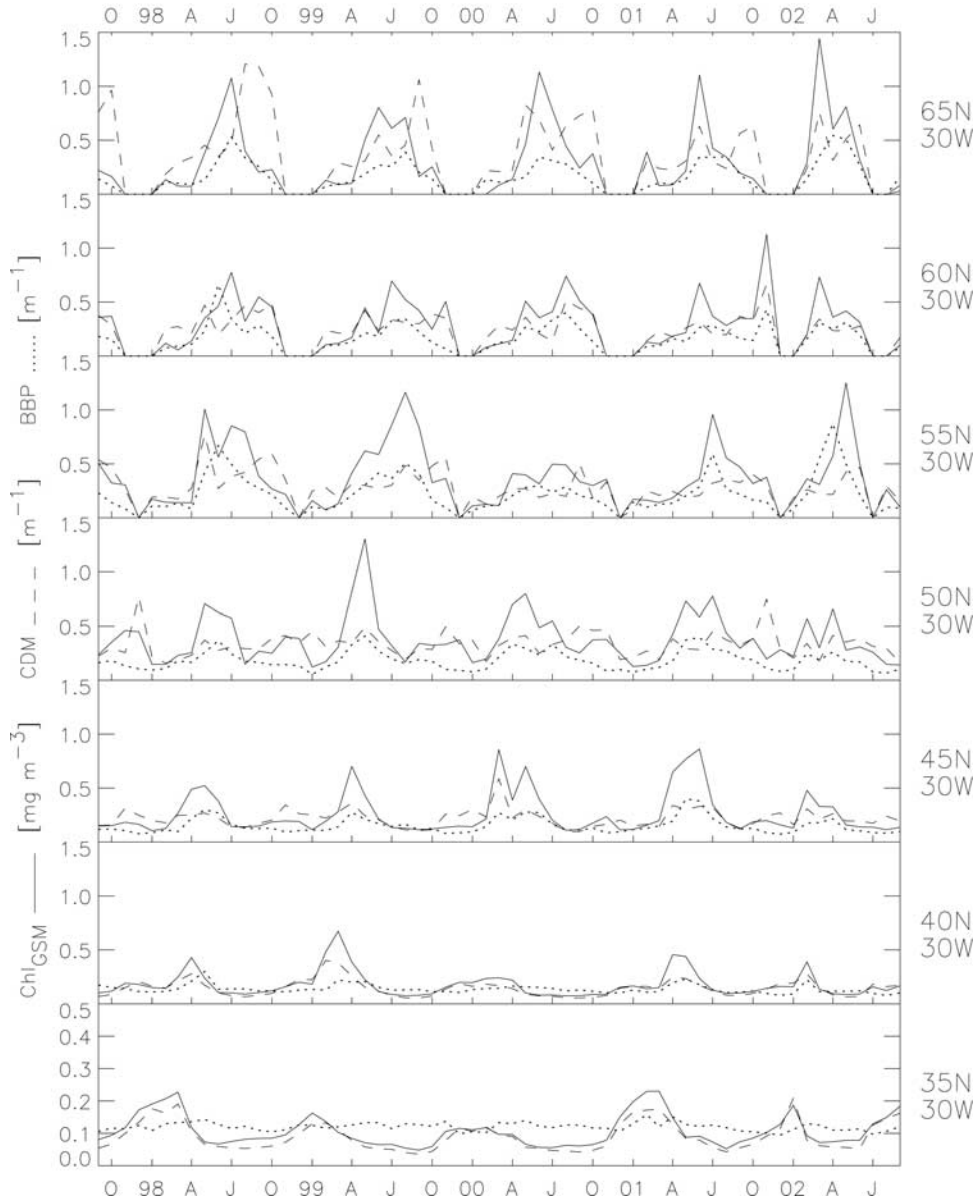

Figure 4. Time series of Chl_{GSM} (solid line), CDM (dashed line), and BBP (dotted line) sampled along a latitudinal gradient across the North Atlantic Basin (along 30°W). The top panel shows the time series at 65°N 30°W and each panel below shows the temporal variability at 35°N 30°W. Values of CDM are scaled by a factor of 10 and BBP by a factor of 100.

the south, cycles in Chl_{GSM} and CDM are more coherent than between Chl_{GSM} and BBP. The relatively featureless time series for BBP south of 40°N, and coincident clear seasonal cycles in Chl_{GSM} suggest strong seasonal changes in phytoplankton physiology (changing phytoplankton C:Chl ratios) in an environment supporting well-matched rates of phytoplankton growth and losses (i.e., sinking, grazing, etc.).

[27] Interannual variations in Chl_{GSM}, BBP, and CDM do not exhibit such clear latitudinal patterns as is observed for the seasonal cycles, but these changes nevertheless are substantial. For example, the strong spring Chl bloom observed at 45°N during 2000 does not correspond to similar events at higher or lower latitudes, and in fact is matched to the lowest amplitude seasonal cycle at 40°N (Figure 4). Interestingly, strong interannual features in one of the three optical properties are not necessarily observed in the other properties, demonstrating that temporal patterns in Chl_{GSM}, CDM, and BBP can vary independently.

[28] Temporal changes in the relative contributions made by CDM and BBP can be diagnosed by evaluating the time courses of %CDM and BBP2APH (Figure 5). For example, values of %CDM at 35°N 30°W peak in the spring and are lower in the fall following Chl_{GSM} patterns, whereas north of 50°N, %CDM values often mirror the observed temporal patterns in Chl_{GSM}. This suggests that in the southern part of the transect (south of 55°N), seasonal mixing, phytoplankton pigmentation, and CDOM cycling all interact to produce a temporal pattern where %CDM decreases during the spring and summer owing to the bleaching of surface waters

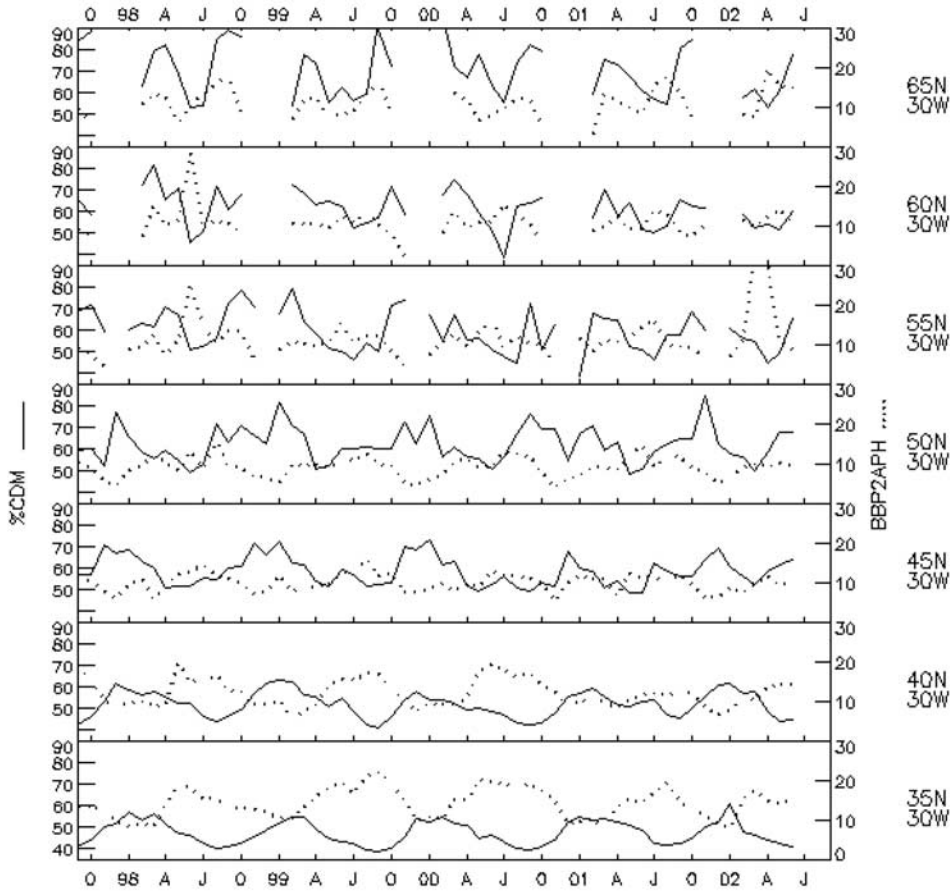

Figure 5. Time series of %CDM (solid line, left *y* axis) and BBP2APH (dotted line, right *y* axis) sampled along a latitudinal gradient across the North Atlantic Basin (along 30°W). The top panel shows the time series at 65°N 30°W and each panel below shows the temporal variability at 35°N 30°W.

while deep mixing in the fall and winter increases values of %CDM dramatically (Figure 5). However, north of 55°N, a different pattern emerges where phytoplankton related processes seem to outweigh others and values of %CDM decrease as Chl increases.

[29] Seasonal changes in BBP2APH also show interesting patterns when viewed across the North Atlantic Ocean (Figure 5). South of 45°N, values of BBP2APH decrease during the bloom, while north of 55°N, there appears to be a slight increase in BBP2APH coherent with the chlorophyll blooms. These two behaviors are consistent with physiological changes in C:Chl ratios regulating BBP2APH values at the southern site and a fairly constant relationship between backscattering and chlorophyll biomass (i.e., biomass control) to the north. Between these two latitudes, values of BBP2APH increase in the leading edge of the bloom, probably modulating the influence of the two above processes linking chlorophyll and particulate biomass indices. In all, BBP2APH shows several interesting patterns that suggest its utility as an index for assessing phytoplankton physiological status [*Behrenfeld et al.*, 2005].

[30] Interannual variations of the three variables are perhaps most clearly illustrated in the equatorial Pacific Ocean during a transition from El Niño to non-El Niño conditions (Figure 6). During the 1997/1998 El Niño at 0°N 140°W (i.e., prior to March 1998), values for all three variables are low, %CDM is ~35%, and BBP2APH is >0.01. A sharp rise in all three ocean color properties is then seen during the subsequent La Niña transition (summer of 1998) in response to enhanced equatorial upwelling, with the rise in CDM and Chl_{GSM} being relatively greater than the change in BBP (Figure 6). Accordingly, BBP2APH decreased across the transition period, reflecting improvements in the physiological status of the phytoplankton community. The %CDM also increased during this period owing to the stimulated supply of subsurface CDM to the mixed layer [*Siegel et al.*, 2002b; *Simeon et al.*, 2003].

3.5. Spatial Patterns in the Temporal Correlation Among Ocean Color Properties

[31] The degree of independent variability among the three central variables can be viewed by examining spatial distributions of the correlation coefficients (r-values) for the monthly-resolved time series (Figure 7). High r values denote where local time series of differing properties are highly correlated. While r values among different sites may be similar, the corresponding slopes can be very different. Values of the correlation coefficient between Chl_{WiFS} and Chl_{GSM} time series are generally quite high (r values are typically greater than 0.8), and there are only a few regions where their correspondence is poor (Figure 7a). These regions of poor correlation include many coastal regions

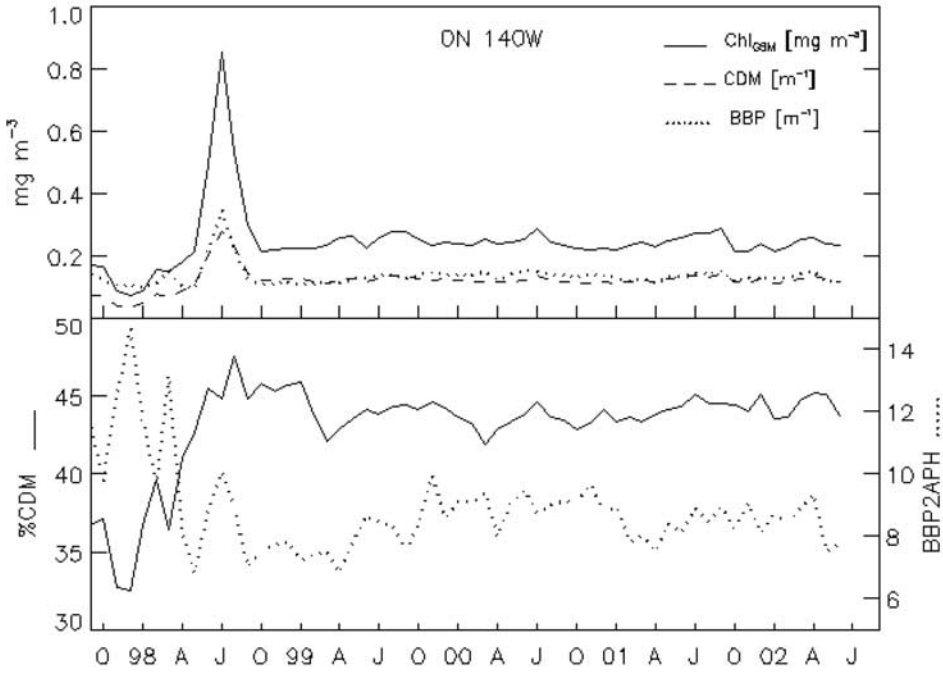

Figure 6. Time/longitude distribution on the equatorial Pacific Ocean (0°N 140°W) for (top) Chl_{GSM} (solid line), CDM (dashed line; multiplied by a factor of 10), and BBP (dotted line; multiplied by a factor of 100) and (bottom) %CDM (solid line) and BBP2APH (dashed line; right *y* axis).

and marginal seas, such as the North Sea, Gulf of Guinea, and portions of the Arabian and Yellow seas. Regions of poor correlation often signal poor atmospheric correction driven by high concentrations of mineral aerosols, such as off northwest Africa [*Moulin et al.*, 2001; *Schollaert et al.*, 2003], or the application of GSM01 in coastal Case II waters where it is not valid.

[32] Correlations between Chl_{GSM} and CDM are highest in the subtropical and tropical regions ($r > 0.7$) and are weakest (even negatively correlated) in large-scale upwelling regions (Figure 7b). High positive correlation coefficients between Chl_{GSM} and CDM indicate that Chl is responding to environmental perturbations (i.e., vertical mixing, incident irradiance, nutrient supply) on timescales similar to changes in the balance of forcing factors controlling CDM (i.e., upwelling of CDOM-rich subsurface waters, photobleaching, changes in heterotrophic production). Weak or even inverse correlation coefficients for

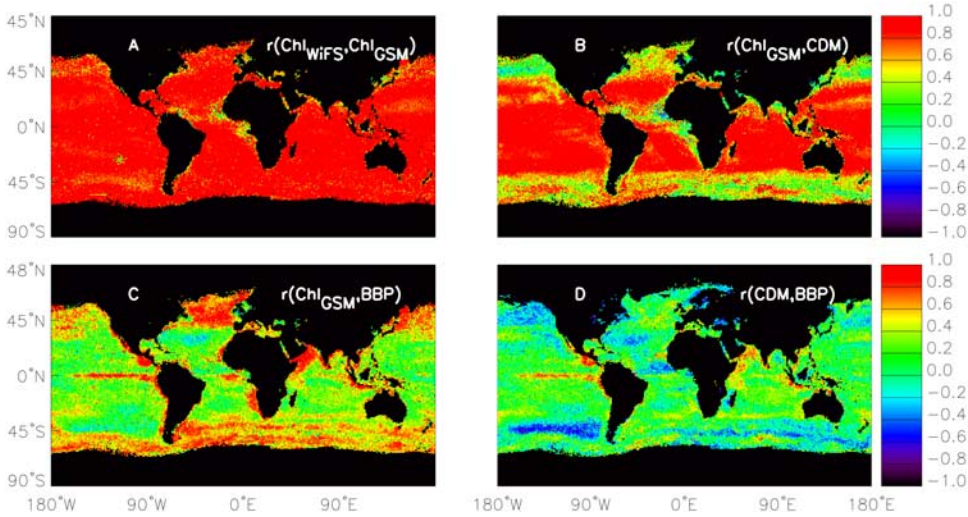

Figure 7. Correlation coefficient (r-values) between (a) CHL_{GSM} and Chl_{WiFS}, (b) CHL_{GSM} and CDM, (c) CHL_{GSM} and BBP, and (d) CDM and BBP. Values of the correlation coefficient are calculated at each point (1° resolution) over the 5-year record. Correlation coefficient values are plotted only if data are available more than one half of the record.

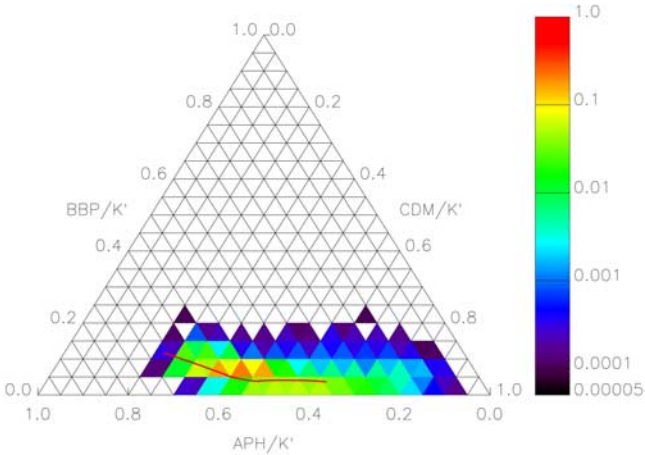

Figure 8. Triangle plot for the contribution that each IOP makes to the non-water light attenuation coefficient at 440 nm (K'; equation (4)). Contributions made by each IOP are 1 at each vertex and the contribution can be read off from axis starting at 1.0 and decreasing from there. For example, the relative contributions from APH are given by the lower axis, for BBP on the left axis and for CDM on the right axis. Superimposed is the space occupied by the bio-optical assumption (red line). Here reflectance spectra are determined using the bio-optical model of *Morel and Maritorena* [2001] for chlorophyll concentrations ranging from 0.01 to 10 mg m^{-3} and then used as input for the GSM01 semi-analytical model. The highest value of Chl is found on the right-hand side of the solid red line.

Chl_{GSM} and CDM indicate a temporal decoupling of these processes. Regions of weak or negative correlation include the Subarctic North Pacific, the Subarctic North Atlantic, and much of the Southern Ocean, as well as some marginal seas and coastal waters (Figure 7b). However, not all marginal seas follow this pattern (compare the Mediterranean Sea and Gulf of Mexico). An interesting feature in the global correlation map for Chl and CDM is that the mean paths of the Kuroshio and Gulf Stream appear to demarcate regions of high and low correlation (Figure 7b). The most negative correlations are found off West Africa, equatorial Atlantic Ocean, the eastern seaboard of the United States, in the Japan and East China seas, and the Baltic Sea. For these regions, low correlation coefficients reflect the influence of terrestrial inputs or the effects of anomalous atmospheric optical properties. However, terrestrial influences are largely coastally restricted and CDM is poorly correlated with SeaWiFS-derived aerosol properties, such as aerosol optical thickness or Angstrom exponent (not shown).

[33] For Chl_{GSM} and BBP, correlation coefficients are high ($r > 0.6$) throughout the subarctic gyres, the Southern Ocean, coastal areas, and equatorial upwelling regions (Figure 7c). This correspondence reflects the dominating influence of changes in phytoplankton biomass on both BBP and Chl. Values of Chl_{GSM} and BBP are poorly correlated for much of the subtropical ocean (Figure 7c). There, changes in Chl_{GSM} largely reflect physiological acclimations to changing light and nutrient conditions while tightly coupled phytoplankton growth and grazing minimizes variability in phytoplankton carbon biomass [see also *Behrenfeld et al.*, 2005].

[34] Correlation coefficients between CDM and BBP are generally low and often negative (Figure 7d). High positive correlations ($r > 0.6$) are found for the equatorial Pacific, West Indian Ocean, the Costa Rica dome, Antarctic shelf regions, and the Arabian Sea. Strong upwelling of nutrient- and CDOM-rich waters can lead to a positive BBP-CDM correlation as is seen in several of these regions (Figure 7d). The correspondence is not as widespread as is observed with the correlation between Chl_{GSM} and BBP (Figure 7c), suggesting that the differences between these correlation distributions may be a way to differentiate between regions of strong and weak upwelling.

4. Discussion

[35] The simultaneous retrieval of multiple ocean color properties from SeaWiFS imagery provides new understanding of the global distribution of ocean optical quantities and their spatial-temporal variations. With these data, we can evaluate and partition the independent and interdependent behaviors on global and climatological scales. In the following, we visualize the relative contribution of the three ocean color properties using a ternary plot and then begin the process of synthesizing our results toward an understanding of the regulating processes and environmental forcing factors responsible for the observed behaviors. Last, we use these understandings to re-evaluate the bio-optical assumption and its applicability.

4.1. A Ternary Representation of Global Ocean Color Properties

[36] A common way of looking at three component relationships is with a ternary (or triangle) plot. The shorter the perpendicular distance between a vertex and a point in triangular space, the greater the relative importance of the factor represented by the vertex. Ternary plots have long been used as conceptual models for ocean color variability [*International Ocean-Colour Coordinating Group* (*IOCCG*), 2000] but have been rarely used quantitatively. To use a ternary plot the properties to be represented, Chl, CDM, and BBP, must be cast in a way such that their sum equals 1. Fortunately, the single scatter approximation for the diffuse attenuation coefficient, $K_d(\lambda)$, provides a convenient way of doing this normalization. That is, the non-water diffuse attenuation coefficient at 440 nm, K', can be modeled as

$$K_d(440) - K_w(440) \equiv K' \cong \hat{a}_{ph}(440; \mathrm{Chl_{GSM}}) + \mathrm{CDM} = \mathrm{BBP}, \quad (4)$$

where $K_w(\lambda)$ is the pure seawater component of diffuse attenuation and $\hat{a}_{ph}(440;Chl_{GSM})$ is modeled as before. By normalizing by the sum of three constituents using K', we can assess the role that each provides to the vertical attenuation of solar radiation at 440 nm.

[37] A density plot representing the frequency of occurrence of the three ocean color properties in ternary space is presented in Figure 8. Clearly, non-water solar attenuation is dominated by contributions from phytoplankton and CDM, with BBP playing a much smaller role. Most frequently, the

Table 4. Interdependence and Independence of Ocean Color Properties by Biome

Biomes	Forcings	Correlated Ocean Color Properties	Independent Ocean Color Properties	Cluster Number in Figure 9
Subtropical gyres	large-scale downwelling; high irradiance	Chl-CDM	BBP	2
Subarctic gyres and Southern Ocean	large-scale upwelling; high vertical mixing; low irradiance	BBP-Chl	CDM	4, 5, 6
Equatorial upwelling	regionally intense upwelling; low vertical mixing; high irradiance	BBP-Chl-CDM		3
Coastal upwelling	regionally intense upwelling; low vertical mixing; moderate irradiance	BBP-Chl-CDM		4
Land influence	riverine inputs of high sediment and/or CDOM	BBP-CDM	Chl	7

contribution of BBP to *K*' is less than 10% while Chl and CDM both contribute in the 40 to 50% range. Only rarely does the BBP contribution become greater than 20%. Overall, Chl makes a slightly larger contribution to *K*' than CDM (Figure 8), although CDM contributions are always important. Interestingly, the ternary plot identifies waters that are clearly CDM dominated (CDM contributions are >80%), whereas no cases are found where Chl dominates to the same degree.

[38] Superimposed on this ternary plot are the spaces occupied by the bio-optical assumption (red line in Figure 8). Here reflectance spectra from the bio-optical model of *Morel and Maritorena* [2001] for chlorophyll concentrations ranging from 0.01 to 10 mg m^{-3} are used as inputs for the GSM01 model and then plotted on the ternary plot. The graphical region occupied by the bio-optical model corresponds well to the most probable occurrences found in the satellite observations. This is expected because both models use simple fits to similar global data sets [*Morel and Maritorena*, 2001; *Maritorena et al.*, 2002]. Interestingly, the higher the chlorophyll concentration applied to the bio-optical model, the lower the chlorophyll contribution to *K*' and the greater that of CDM in the ternary plot. Furthermore, the BBP contribution to *K*' is almost constant.

4.2. Classification of the Regional Responses to Environmental Forcings

[39] The three ocean color properties retrieved here exhibit patterns that demonstrate regulation by environmental forcings which control mixed layer light climate, exchanges between the mixed layer and the ocean thermocline, land-ocean interactions, and possibly others (see Table 1). This can be best diagnosed by examining the regional variations in the linear correlation coefficients between pairs of ocean color properties (Figures 7a–7d). For example, high correlation coefficients are observed between Chl and CDM in the subtropical gyres, while correlations are comparatively absent between Chl and BBP and between CDM and BBP (Table 4). This indicates that similar physical processes regulate changes in Chl and CDM in these regions, but BBP is controlled by other factors. This is consistent with physiological processes altering values of Chl (and thereby C:Chl ratios) and the coupled cycle of photobleaching, production, and vertical mixing regulating CDOM concentrations. High light levels in the subtropical mixed layers result in reduced values of Chl via photoacclimation and CDOM by photolysis as well as decreased diffusive fluxes of new material from depth (either in the form of newly produced CDOM or new nutrients). Values of BBP are affected by these processes to a much smaller degree, hence its apparent independence in these regions (Table 4).

[40] Contrasting the subtropical gyres are the subarctic gyres, where a good correspondence is observed between Chl and BBP but very little correlation is found between CDM and BBP or Chl (Figure 7). Compared with the subtropical gyres, incident solar fluxes are reduced and mixed layer depths are much greater in the subarctic gyres. Hence the role of photolysis on CDM is likely dampened. Rates of vertical exchange, on the other hand, are greatly enhanced and bring new nutrients to the surface that support increased phytoplankton biomass and thus parallel changes in Chl and BBP. This is illustrated in the time series of Chl and BBP north at 45°N along 30°W (Figures 1 and 4) where new nutrient inputs couple Chl and BBP owing to increases in phytoplankton abundance, while CDM remains decoupled owing to lower light levels and (presumably) reduced rates of CDOM photobleaching (Table 4).

[41] All three ocean color properties show good correspondence for the eastern equatorial Pacific Ocean (Figure 7). This region may be characterized by high incident irradiance levels and intense vertical equatorial upwelling. Accordingly, upwelling brings new nutrients (increasing BBP and Chl) and increased concentrations of CDOM, while intense solar fluxes act to reduce Chl and CDM in roughly similar ways. Consequently, all three properties are functionally interconnected. Alternative mechanisms for variables coupling and uncoupling in other regions are listed in Table 4, which illustrates (albeit qualitatively) the consistency between regional forcings and the responses of the three variables.

[42] An objective way to address common features among the three retrievals is through cluster analysis [e.g., *Everitt et al.*, 2001]. Cluster analysis is a multivariate analysis technique that organizes information about variables and then forms homogeneous groups (or "clusters") from this information. Groups created in this manner are highly homogenous internally (members of a group are similar to one another) and highly heterogeneous externally (members of a group are not like members of other groups). In a cluster analysis, each sample (i.e., each pixel of a global map) is assigned to a unique group based upon the values of its corresponding variables (Chl, CDM, and BBP) through the minimization of a distance criterion based upon the variable inputs. In the current case, the three variables of interest had different scales, so the Chl, CDM, and BBP

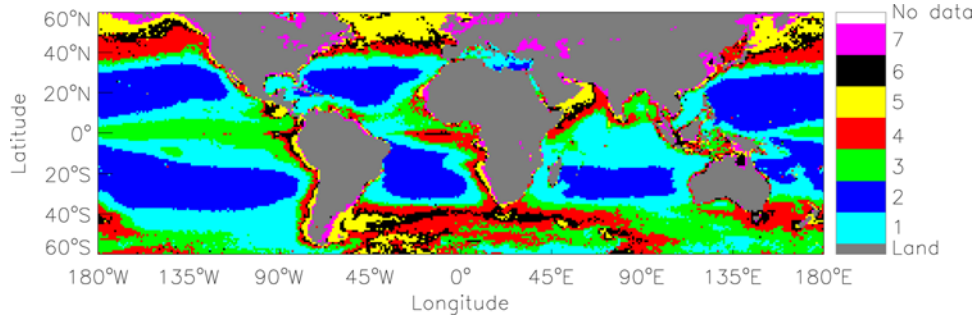

Figure 9. Cluster analysis results for the climatological Chl, CDM, and BBP fields for the region between 60°S and 60°N. The cluster analysis is constrained to produce seven classes, and the data are $\log_{10}$ transferred before analysis. The classes are ordered by their fraction of total ocean area covered. Fractional coverages for the classes are in order 26, 24, 18, 15, 7, 6, and 3% for classes 1 to 7, respectively.

data were log-transformed and the analysis was constrained to create seven groups (Figure 9). The cluster regions diagnosed here is similar in many ways to the empirical regionalization created by A. Longhurst and collaborators [e.g., *Longhurst*, 1998] as well as the variance analyses of *Esaias et al.* [1999].

[43] The seven ocean color property cluster classes are ordered by the areal contribution each makes to the total ocean area between 60°N and 60°S (Figure 9). Class 2 makes up 24% of the valid ocean pixels and represents the clearest waters of the subtropical gyres. Classes 4, 6, and 5 represent regions of ever-increasing upwelling and other nutrient inputs contributing 15, 7, and 6% of the total ocean area, respectively. Cluster group 1 makes the largest contribution to the total ocean area (26%) and represents a transition between oligotrophic conditions and upwelling regions. The third class is unique to the equatorial regions and portions of the Southern Ocean and makes up 18% of the ocean. The seventh class represents marginal and inland seas and makes up only 3% of the total ocean (Figure 9).

[44] The various cluster classes can be related to the qualitative discussion of ocean color property interrelationships described previously (Table 4). For example, in subtropical gyres, values of BBP are roughly independent of the coupled variations in Chl and CDM and this relationship covers roughly 25 to 50% of the ocean (depending on how much of cluster 1 is accounted for in this mode). High-latitude, upwelling systems where BBP and Chl are coupled and yet CDM remains independent cover 25 to 30% of the ocean surface (Table 4). Equatorial ecosystems (possibly all HNLC regions) are contained mostly by cluster 3 which makes up 18% of the ocean. For these regions, all three properties are highly related. Coastal upwelling regions have similar relationships though they cover an even smaller portion of the ocean. Last, regions with significant land influences on ocean color properties make up only 3% of the total ocean. The present analysis is not perfect, and more work is required to provide a quantitative resolution of the hypotheses we have just stated. However, the combination of the interpretation of the cluster analysis (Figure 9) and the correlation maps (Figure 7) provides a first-order assessment of regional independence and interdependencies of ocean color properties.

4.3. On the Bio-Optical Assumption

[45] The analyses and interpretations of independent and interdependent behaviors of the retrieved ocean color properties presented here bring us back to the bio-optical assumption. When evaluated using multiple optical properties across a broad range of space and timescales, there are obvious inconsistencies with the bio-optical assumption. The fact that such a simple description does not hold over all time and space scales should not be surprising as these inconsistencies have driven researchers to develop more complete descriptions of ocean color properties. Importantly, deviations from the bio-optical assumption are consistent with our current understanding of how the independent forcings control the fundamental ocean color properties, Chl, CDM, and BBP. The manifestation of these interactions is distributed over space and time as controlled by regional environmental forcings. These results call for the development of a more comprehensive bio-optical framework that encompasses (at least) a three-component parameter space. The general characteristics of this three-parameter approach can be visualized by evaluating the relative contributions of Chl, BBP, and CDM to ocean color spectra. In such a way, we hope that the field of ocean color remote sensing will emerge from its monochromatic view of the ocean biosphere (chlorophyll alone) to a more multihued view enabling multiple biospheric processes to be diagnosed simultaneously.

[46] **Acknowledgments.** The authors gratefully acknowledge NASA and the NSF for support of their work on global ocean color remote sensing and its interpretation. Manuela Lorenzi-Kayser ably performed the calculations presented here. The reviewers and editors are thanked for their useful comments. Last, the Orbimage Corporation and the SeaWiFS Project at the NASA Goddard Space Flight Center are thanked for providing the SeaWiFS ocean color data set to the research and education community.

References

Bader, H. (1970), The hyperbolic distribution of particle sizes, *J. Geophys. Res.*, *75*, 2822–2830.

Behrenfeld, M. J., and E. Boss (2003), The beam attenuation to chlorophyll ratio: An optical index of phytoplankton photoacclimation in the surface ocean?, *Deep Sea Res., Part I*, *50*, 1537–1549.

Behrenfeld, M. J., E. Marañon, D. A. Siegel, and S. B. Hooker (2002), Photoacclimation and nutrient-based model of light-saturated photosynthesis for quantifying oceanic primary production, *Mar. Ecol. Prog. Ser.*, *228*, 103–117.

Behrenfeld, M. J., E. Boss, D. A. Siegel, and D. M. Shea (2005), Global remote sensing of phytoplankton physiology, *Global Biogeochem. Cycles*, *19*, GB1006, doi:10.1029/2004GB002299.

Boyd, P. W. (2002), The role of iron in the biogeochemistry of the Southern Ocean and equatorial Pacific: A comparison of in situ iron enrichments, *Deep Sea Res., Part II*, *49*, 1803–1821.

Bricaud, A., A. Morel, M. Babin, K. Allali, and H. Claustre (1998), Variations of light absorption by suspended particles with the chlorophyll a concentration in oceanic (case 1) waters: Analysis and implications for bio-optical models, *J. Geophys. Res.*, *103*, 31,033–31,044.

Brown, C. W., and J. A. Yoder (1994), Coccolithophorid blooms in the global ocean, *J. Geophys. Res.*, *99*, 7467–7482.

Carder, K. L., S. K. Hawes, R. C. Smith, R. G. Steward, and B. G. Mitchell (1991), Reflectance model for quantifying chlorophyll a in the presence of productivity degradation products, *J. Geophys. Res.*, *96*, 20,599–20,611.

Carder, K. L., F. P. Chen, Z. P. Lee, S. Hawes, and D. Kamykowski (1999), Semi-analytic MODIS algorithms for chlorophyll *a* and absorption with bio-optical domains based on nitrate-depletion temperatures, *J. Geophys. Res.*, *104*, 5403–5421.

Chomko, R. M., H. R. Gordon, S. Maritorena, and D. A. Siegel (2003), Simultaneous retrieval of oceanic and atmospheric parameters for ocean color imagery by spectral optimization: A validation, *Remote Sens. Environ.*, *84*, 208–220.

Claustre, H., and S. Maritorena (2003), The many shades of ocean blue, *Science*, *302*, 1514–1515.

Esaias, W. E., R. L. Iverson, and K. Turpie (1999), Ocean province classification using ocean colour data: Observing biological signatures of variations in physical dynamics, *Global Change Biol.*, *6*, 39–55.

Everitt, B. S., S. Landau, and M. Leese (2001), *Cluster Analysis*, 4th ed., 248 pp., Edward Arnold, London.

Falkowski, P. G. (1984), Physiological responses of phytoplankton to natural light regimes, *J. Plankton Res.*, *6*, 295–307.

Fennel, K., and E. Boss (2003), Subsurface maxima of phytoplankton and chlorophyll—Steady state solutions from a simple model, *Limnol. Oceanogr.*, *48*, 1521–1534.

Garver, S. A., and D. A. Siegel (1997), Inherent optical property inversion of ocean color spectra and its biogeochemical interpretation: 1. Time series from the Sargasso Sea, *J. Geophys. Res.*, *102*, 18,607–18,625.

Geider, R. J., H. L. MacIntyre, and T. Kana (1998), A dynamic regulatory model of phytoplanktonic acclimation to light, nutrients, and temperature, *Limnol. Oceanogr.*, *43*, 679–694.

Gordon, H. R., and A. Morel (1983), Remote assessment of ocean color for interpretation of satellite visible imagery, in *Lecture Notes on Coastal and Estuarine Studies*, edited by R. T. Barber et al., pp. 1–113, Springer, New York.

International Ocean-Colour Coordinating Group (2000), *Remote Sensing of Ocean Colour in Coastal, and Other Optically-Complex Waters*, edited by S. Sathyendranath, Dartmouth, N. S., Canada.

Kahru, M., and B. G. Mitchell (1999), Empirical chlorophyll algorithm and preliminary SeaWiFS validation for the California Current, *Int. J. Remote Sens.*, *20*, 3423–3429.

Kitchen, J. C., and J. R. V. Zaneveld (1990), On the non-correlation of the vertical structure of light scattering and chlorophyll *a* in Case I waters, *J. Geophys. Res.*, *95*, 20,237–20,246.

Loisel, H., and A. Morel (1998), Light scattering and chlorophyll concentration in case 1 waters: A reexamination, *Limnol. Oceanogr.*, *43*, 847–858.

Loisel, H., J. M. Nicolas, P. Y. Deschamps, and R. Frouin (2002), Seasonal and inter-annual variability of the particulate matter in the global ocean, *Geophys. Res. Lett.*, *29*(24), 2196, doi:10.1029/2002GL015948.

Longhurst, A. (1998), *Ecological Geography of the Sea*, 398 pp., Elsevier, New York.

Maritorena, S., and D. A. Siegel (2005), Consistent merging of satellite ocean color data using a semi-analytical model, *Remote Sens. Environ.*, *94*, 429–440.

Maritorena, S., D. A. Siegel, and A. Peterson (2002), Optimization of a semi-analytical ocean color model for global scale applications, *Appl. Opt.*, *41*, 2705–2714.

McClain, C. R., G. C. Feldman, and S. B. Hooker (2004), An overview of the SeaWiFS project and strategies for producing a climate research quality global ocean bio-optical time series, *Deep Sea Res., Part II*, *51*, 5–42.

Morel, A., and Y.-H. Ahn (1991), Optics of heterotrophic nanoflagellates and ciliates: A tentative assessment of their scattering role in oceanic waters compared with bacterial and algal cells, *J. Mar. Res.*, *49*, 1–26.

Morel, A., and S. Maritorena (2001), Bio-optical properties of oceanic waters: A reappraisal, *J. Geophys. Res.*, *106*, 7163–7180.

Moulin, C., H. R. Gordon, R. M. Chomko, V. F. Banzon, and R. H. Evans (2001), Atmospheric correction of ocean color imagery through thick layers of Saharan dust, *Geophys. Res. Lett.*, *28*, 5–8.

Nelson, N. B., and D. A. Siegel (2002), Chromophoric DOM in the open ocean, in *Biogeochemistry of Marine Dissolved Organic Matter*, edited by D. A. Hansell and C. A. Carlson, pp. 547–578, Elsevier, New York.

Nelson, N. B., D. A. Siegel, and A. F. Michaels (1998), Seasonal dynamics of colored dissolved material in the Sargasso Sea, *Deep Sea Res., Part I*, *45*, 931–957.

Nelson, N. B., C. A. Carlson, and D. K. Steinberg (2004a), Production of chromophoric dissolved organic matter by Sargasso Sea microbes, *Mar. Chem.*, *89*, 273–287.

Nelson, N. B., D. A. Siegel, and J. A. Yoder (2004b), The spring bloom in the Sargasso Sea: Spatial extent and relationship with winter mixing, *Deep Sea Res., Part II*, *51*, 987–1000.

O'Reilly, J. E., S. Maritorena, B. G. Mitchell, D. A. Siegel, K. L. Carder, S. A. Garver, M. Kahru, and C. R. McClain (1998), Ocean color chlorophyll algorithms for SeaWiFS, *J. Geophys. Res.*, *103*, 24,937–24,953.

Otero, M. P., and D. A. Siegel (2004), Spatial and temporal characteristics of sediment plumes and phytoplankton blooms in the Santa Barbara Channel, *Deep Sea Res., Part II*, *51*, 1139–1149.

Roesler, C. S., and M. J. Perry (1995), In situ phytoplankton absorption, fluorescence emission, and particulate backscattering spectra determined from reflectance, *J. Geophys. Res.*, *100*, 13,279–13,294.

Schollaert, S. E., J. A. Yoder, J. E. O'Reilly, and D. L. Westphal (2003), Influence of dust and sulfate aerosols on ocean color spectra and chlorophyll *a* concentrations derived from SeaWiFS off the U.S. east coast, *J. Geophys. Res.*, *108*(C6), 3191, doi:10.1029/2000JC000555.

Siegel, D. A., and A. F. Michaels (1996), On non-chlorophyll light attenuation in the open ocean: Implications for biogeochemistry and remote sensing, *Deep Sea Res., Part II*, *43*, 321–345.

Siegel, D. A., S. C. Doney, and J. A. Yoder (2002a), The North Atlantic spring phytoplankton bloom and Sverdrup's critical depth hypothesis, *Science*, *296*, 730–733.

Siegel, D. A., S. Maritorena, N. B. Nelson, D. A. Hansell, and M. Lorenzi-Kayser (2002b), Global distribution and dynamics of colored dissolved and detrital organic materials, *J. Geophys. Res.*, *107*(C12), 3228, doi:10.1029/2001JC000965.

Simeon, J., C. S. Roesler, W. S. Pegau, and C. Dupouy (2003), Sources of spatial variability in light absorbing components along an equatorial transect from 165°E to 150°W, *J. Geophys. Res.*, *108*(C10), 3333, doi:10.1029/2002JC001613.

Smith, R. C., and K. S. Baker (1978a), The bio-optical state of ocean waters and remote sensing, *Limnol. Oceanogr.*, *23*, 247–259.

Smith, R. C., and K. S. Baker (1978b), Optical classification of natural waters, *Limnol. Oceanogr.*, *23*, 260–267.

Stramski, D., and D. A. Kiefer (1991), Light scattering by microorganisms in the open sea, *Prog. Oceanogr.*, *28*, 343–383.

Stramski, D., R. A. Reynolds, M. Kahru, and B. G. Mitchell (1999), Estimation of particulate organic carbon in the ocean from satellite remote sensing, *Science*, *285*, 239–242.

Stramski, D., E. Boss, D. Bogucki, and K. J. Voss (2004), The role of seawater constituents in light backscattering in the ocean, *Prog. Oceanogr.*, *61*, 27–55.

Sverdrup, H. U. (1953), On conditions for the vernal blooming of phytoplankton, *J. Cons. Cons. Int. Explor. Mer.*, *18*, 287–295.

Sverdrup, H. U. (1955), The place of physical oceanography in oceanographic research, *J. Mar. Res.*, *14*, 287–294.

Yoder, J., C. R. McClain, G. C. Feldman, and W. E. Esaias (1993), Annual cycles of phytoplankton chlorophyll concentrations in the global ocean: A satellite view, *Global Biogeochem. Cycles*, *7*, 181–193.

M. J. Behrenfeld, Department of Botany and Plant Pathology, Oregon State University, Corvallis, OR 97331-2902, USA.

S. Maritorena, N. B. Nelson, and D. A. Siegel, Institute for Computational Earth System Science, University of California, Santa Barbara, Santa Barbara, CA 93106-3060, USA. (davey@icess.ucsb.edu)